Bidirectional LCLL Resonant Converter With Wide Output Voltage Range

Yi Zhang, Donglai Zhang, *Senior Member, IEEE*, Jie Li, and Hongyu Zhu

***Abstract*—A new bidirectional LCLL-type resonant dc-dc converter (LCLL-BDC) is proposed in this article, which features a wide output voltage range for both ports, thus achieving zero-voltage switching (ZVS) at the input side and zero-current switching (ZCS) at the output side. The snubberless converter is similar to the type-11 LLC-type resonant converter, with the exception of an additional inductor. The auxiliary inductor allows for the converter to achieve a wide voltage range power transfer, thus addressing the inability of the LLC-type converter to be boosted in the reverse mode. The equivalent model and the steady-state operation are presented in this article. Moreover, the design methodology for the resonant network was derived for the LCLL-BDC. A 1-kW prototype, which interfaces two batteries of different energy systems, was developed to verify the validity and applicability of the proposed converter. The input and output voltage range was found to be 80–120 V, and the highest efficiencies for the bidirectional operational modes exceeded 96%.**

***Index Terms*—Battery, bidirectional dc–dc converter (BDC), resonant tank, wide output voltage range.**

I. Introduction

With an increase in the research attention directed toward renewable power systems with storage units, bidirectional dc-dc converters (BDCs) that are capable of interfacing and controlling bidirectional power terminals with a wide voltage range and high efficiency are required. The BDCs play an important roles in uninterrupted power supplies (UPSs), electric vehicles (EVs), plug-in hybrid electric vehicles (PHEVs), and aviation power systems. Besides, energy transfer between distributed energy systems (DESs) can be realized by adding the BDCs. Typically, the port of the BDCs is connected to the bus or an energy storage device such as a battery or a super capacitor, and it therefore can interface energy from a bus or energy storage device.

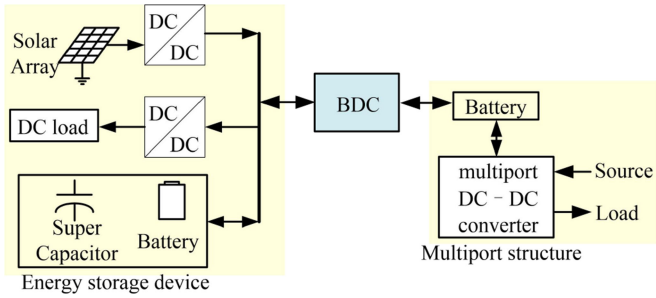

Fig. 1. Application of BDCs.

Bidirectional dc-dc converters (BDCs) can be divided into two types: isolated converters and non-isolated converters. Galvanic isolation is typically achieved between different systems using isolation topologies [1], [2]. The most widely-used isolated BDCs are the dual-active-bridge (DAB) converter [3] and bidirectional resonant converter (BRC). However, the soft-switching range and the circulating current inside the DAB converter limit the DAB converter to maintain high efficiency over a wide gain range [4], [5], attracting researches making efforts to improve efficiency and power density [3]. In terms of control methods of DAB, it has evolved from traditional single-phase-shift (SPS) control to extended-phase-shift (EPS), dual-phase-shift (DPS) controls and triple-phase-shift (TPS) control [6]–[9]. While improving the efficiency of the converter, the control becomes more and more complicated. And the reported efficiency performance of DAB converter is still inferior to resonant-type BRCs [10].

In battery charging applications, the battery voltage varies significantly throughout the charging process, and the input voltage and output voltage ranges of the bidirectional converter are significantly wide, such as application shown in Fig. 1, connecting two distributed systems. However, in the wide voltage range application, the performance of BRCs is typically not maximized. In recent years, many researches focus on how to realize the wide voltage range of resonant converter. Methods include changing the resonant tank [11]–[14], adding switches to the front stage, inverter side or rectifier side to increase the switching stages [15]–[17], adding transformer winding [18], adding resonance branches [19], and using novel control methods or modulation methods [20]. In [21], the resonant tank is changed by adding the windings of the transformer to harvest high efficiency and good voltage gain feature. This article mainly

Manuscript received September 1, 2019; revised December 2, 2019 and February 9, 2020; accepted March 25, 2020. Date of publication April 12, 2020; date of current version July 20, 2020. This work was supported in part by the National Natural Science Foundation of China under Grant 51777041, in part by the Shenzhen Science and Technology Plan Project under Grant JCYJ20170413112018620, and in part by the Natural Science Foundation of Guangdong Province, China, under Grant 2019A1515011480. Recommended for publication by Associate Editor T. Mishima. *(Corresponding author: Donglai Zhang.)*

Yi Zhang and Donglai Zhang are with the Power Electronic and Motion Control Research Center, Shenzhen Graduate School of Harbin Institute of Technology, Shenzhen 518055, China (e-mail: zhangyi3017@yeah.net; zhangdonglai@hit.edu.cn).

Jie Li is with the State Grid Jiangxi Nanchang Power Supply Company, Nanchang 330000, China (e-mail: 2921535207@qq.com).

Hongyu Zhu is with the Shenzhen Academy of Aerospace Technology, Shenzhen 518057, China (e-mail: zhuhongyu505@163.com).

Color versions of one or more of the figures in this article are available online at http://ieeexplore.ieee.org.

Digital Object Identifier 10.1109/TPEL.2020.2986505

discusses the method of changing the structure of the resonant cavity without adding the windings of the transformer. This is because the method does not add the switches or change the transformer, and it's simple the control.

Bidirectional series resonant converter (SRC) was studied early. Most of the SRC modulation methods are PFM [22]–[26], called DBSRC (Dual Bridge SRC) which has the same structure as the DAB with a capacitor Cr. There are still large resonance components of current waveform controlled by PFM which bring more core loss. In [27], the calculated efficiency of SRC and DBSRC is summarized. In the high power range, the frequency conversion modulation can achieve more effective converter utilization. However, due to the increase of switching frequency, the efficiency of the converter decreases at low output power. Bidirectional inductor-inductor-capacitor (LLC) resonant dc-dc converters can achieve ZVS and ZCS in almost all load ranges. Therefore, it is also a good choice. However, this topology is still SRC during reverse operation [13].

In [27], two four-resonator topologies were named after "MT-4 CLLC" (Modified Type 4 CLLC), and "MT-11 CLLC" (Modified Type 11 CLLC). The additional capacitor changes the voltage gain characteristics. The voltage gain curve has two the peaks, which are located on both sides of the normalized frequency $f_s/f_r = 1$. Compared with the original T-4 LLC and T-11 LLC, both the dc gains of MT-4 and MT-11 modes are smaller. However, the additional capacitor increases the design complexity due to the double peak voltage gain. This limits the range of the switching frequency and leads to a decrease in the forward voltage gain, which narrows the range of the forward output voltage. And this converter shows different operations between forward and backward power conversion mode because of the transformer's asymmetric turn numbers and the asymmetric structure of resonant networks [29].

A new symmetric LLC-type resonant network(CLLC or CLLC as a distinction) using a digital control scheme is proposed and used recently [11], [12], [30]. This topology has all the advantages of that LLC converter, and is capable of transferring power in either direction [29]. However, The extra resonant tank increases the cost and volume of the converter, and the voltage gain is reduced compared to the traditional LLC converter. The output voltage cannot be regulated continuously by dead-band control. And the current in the output side has to flow through the body diodes of the switches which may cause high conduction loss [11].

The LLCL or IB-LLC (improved bidirectional LLC resonant) BRC inherits the soft-switching characteristic and working principles of the T-4 LLC [l1], [31]–[33]. The auxiliary inductor renders the forward and backward topologies symmetrical, which simplifies analysis and achieves soft-switching. With the proposed new control scheme, the power flow direction and output power of the proposed converter can be changed automatically and continuously [34]. However, the additional inductor has drawbacks. In particular, the current flowing through the auxiliary inductor increases the conduction loss, which reduces the efficiency of the converter.

Afterwards, some topologies that achieve high gain are also proposed, but all will bring some other losses. In [35], SLLC

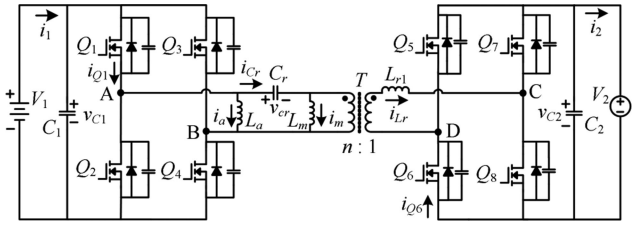

Fig. 2. Proposed BDC and its topology decomposition.

achieves high voltage gain while the adding resonant devices and switches leading more power loss. The CFBRC BRC achieved ZVS because a frequency feed-forward loop is introduced in the battery charging mode [36]. Magnetic components are easier to design than that of LLC but the converter is complex to control. One auxiliary capacitor and two inductors are added to form the buck boost circuits reduce the power density obviously. In [13], the CTLC BRC has a good gain characteristic with ZVS in all load ranges. However, more power loss and more complicated by introducing an auxiliary transformer and an extra capacitance. And the design of magnetic components is more complicated.

Further research is required to satisfy the bidirectional wide voltage range requirements. Besides, this topology should be easily controlled to improve its robustness.

In this paper, a new bidirectional LCLL resonant converter is proposed, which is suitable for wide input and wide output voltage ranges, as shown in Fig. 2. The operating principle is presented in Section II. The theoretical analysis of the proposed topology based on an equivalent model is presented in Section III. Furthermore, the experimental results obtained from a 1-kW prototype are presented to confirm the validity and applicability of the proposed converter in Section IV; followed by a summary of the discussions.

II. Operation Principles

The novel LCLL-type resonant full-bridge topology is shown in Fig. 2. The resonant tank of the proposed converter was derived from Type-11. The body diodes and parasitic capacitances of switches Q_1–Q_8 are shown in Fig. 3, to simplify the analysis of the soft switching. An insulated-gate bipolar transistor (IGBT) with a fly-wheel diode is also suitable for this topology. Besides, the proposed LCLL resonant tank also can be implemented with a half-bridge topology.

The LCLL converter can be controlled using pulse-frequency modulation (PFM) under or above the resonant frequency for both directions of the power flow. Switches positioned at the side of the energy input port, operated at 50% duty cycle and 180° out of phase, act as an inverter; whereas switches at the other side acts as a rectifier. In this study, the primary side was assumed to be the side where L_a is located, thus making the other side the secondary side. For the forward energy delivery, which describes energy flow from the primary side to the secondary side (hereafter, the forward mode), the main principle waveforms are shown in Fig. 3(a), and the four switching modes are shown in Fig. 4. For clarity, the periods of dead time were lengthened. Figs. 3(b) and 5 present the waveforms and switching modes

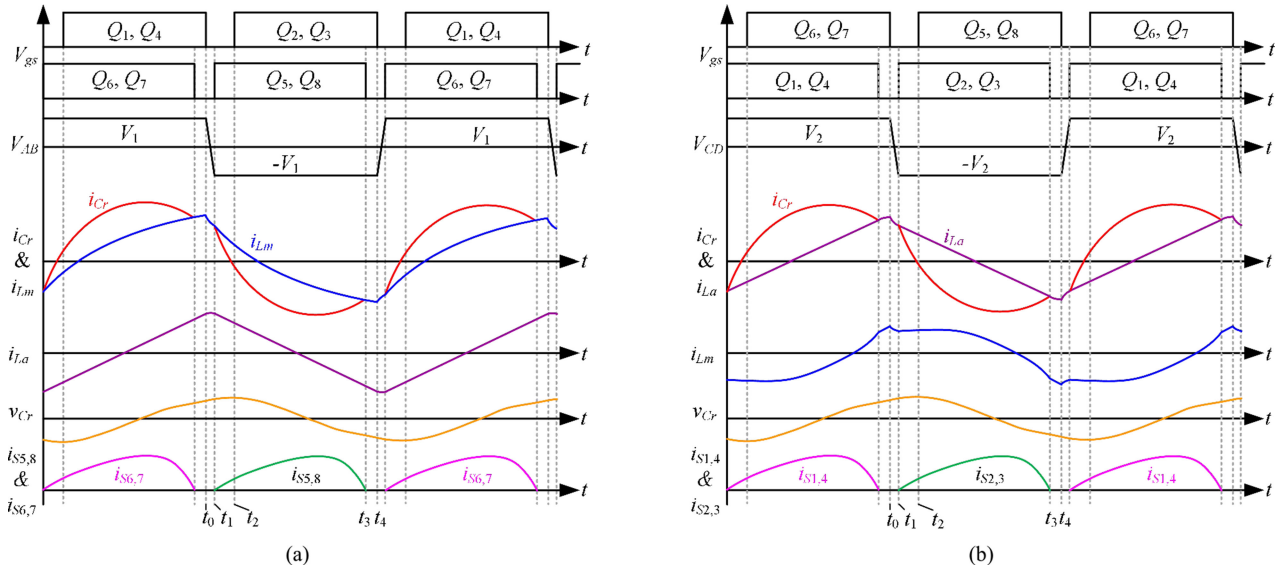

Fig. 3. Operation principles of the proposed LCLL resonant tank. (a) The forward mode ($f_s \leq f_r$). (b) The reverse mode ($f_s \leq f_r$).

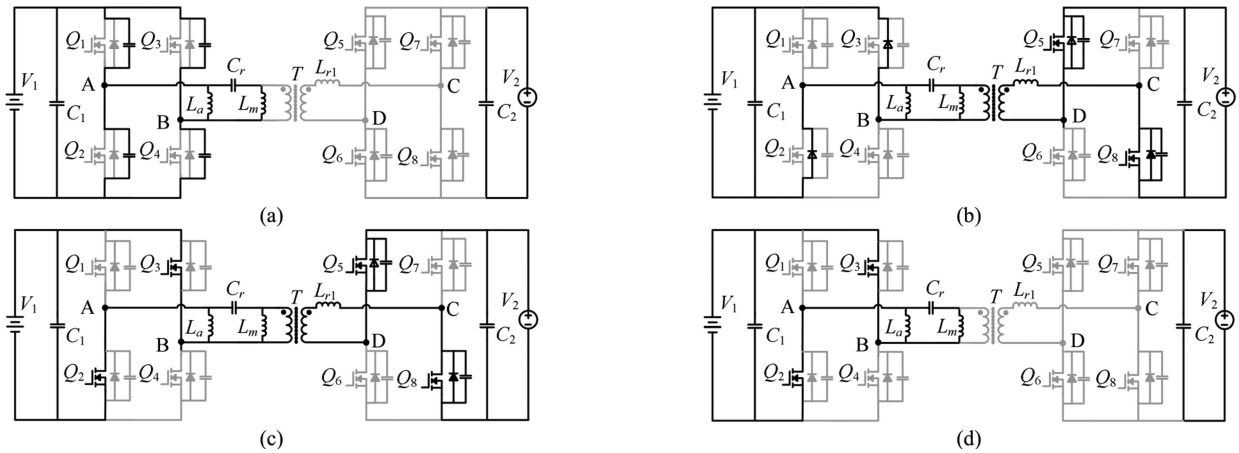

Fig. 4. Equivalent circuits for each stage for half of Switching period in the forward mode. (a) Stage 1. (b) Stage 2. (c) Stage 3. (d) Stage 4.

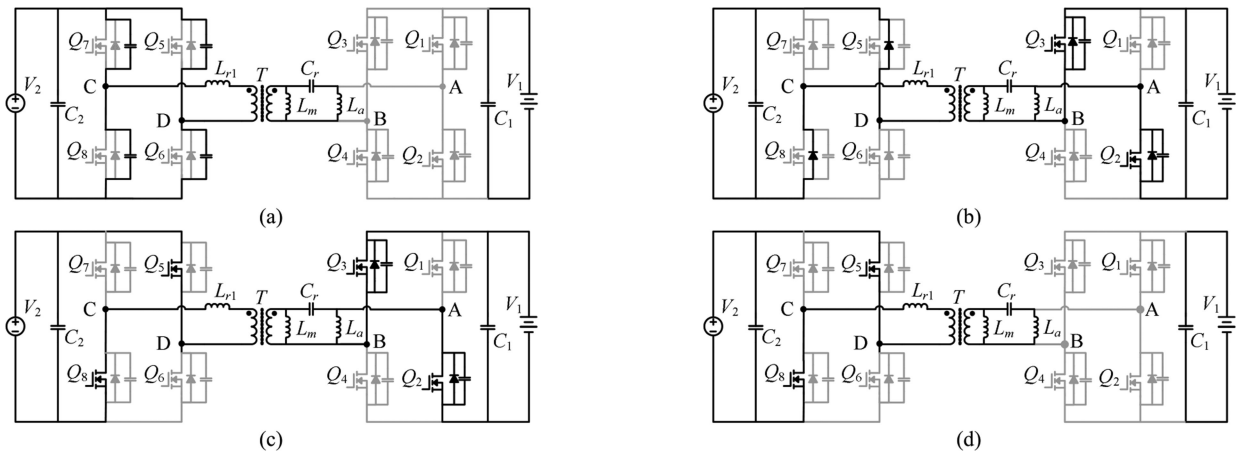

Fig. 5. Equivalent circuits for each stage for half of Switching period in the reverse mode. (a) Stage 1. (b) Stage 2. (c) Stage 3. (d) Stage 4.

of the other energy flow direction (hereafter, the reverse mode). Figs. 4 and 5 present half-cycle equivalent circuits, due to the symmetry of stages, and the corresponding descriptions are not reiterated. All the analyses were based on steady state characteristics, and it was assumed that the transformer magnetizing inductor L_m of the magnetic devices was typically larger than that of the resonant inductance L_r by 3–10 times.

A. Forward Mode

When $f_s \leq f_r$, the forward mode has four stages in each half of the switching cycle:

Stage 1 [t_0, t_1]*:* at time t_0, Q_1 and Q_4 turn off. This interval corresponds to Fig. 4(a) during a dead-time period wherein all the switches are continuously off. The primary current i_{Cr} is equal to i_{Lm} at t_0, which decreases in the positive polarity under the action of the input voltage. During this stage, the parasitic capacitance of power devices C_{Q2} and C_{Q3} are discharging, and C_{Q1} and C_{Q4} are charging through Cr by a portion of i_{Lm}. Given that the value of the parasitic capacitance is smaller than the value of the resonant capacitor C_r, this period is significantly short when compared with the total switching period. At the end of charging and discharging processes, *vds*1, 4 reaches the input voltage and *vds*2, 3 decreases to zero.

Stage 2 [t_1, t_2]*:* at time t_1, the body diode of Q_2 and Q_3 turns on and feeds back into the input source, thus providing the conditions for ZVS switching, as shown in Fig. 4(b). At the same time, the rest of the L_m current $(i_{Lm} - i_{Cr})$ flowing from the primary side of the ideal transformer realizes power forward transmission, and the transformer current of the secondary side continues to flow through Q_5 and Q_8.

Stage 3 [t_2, t_3]*:* at time t_2, Q_2 and Q_3 turn on under ZVS conditions. Given that the auxiliary inductor L_m is clamped by -V_1, the resonant tank is operated as a Type-11 LLC network. And the resonant current i_{Cr} changes in a sinusoidal manner. Before time t_3, i_{Cr} resonates over its peak and decreases. During this stage, the current of the positive side i_{Cr} and i_{Lm} decrease to 0, and the current of the negative side increases. The current $(i_{Cr} - i_{Lm})$ flowing into the primary side of the ideal transformer when $i_{Cr} > i_{Lm}$ continues in forward energy transmission, and the secondary side current flows through Q_5 and Q_8. The equivalent circuit of this mode is shown in Fig. 4(c).

Stage 4 [t_3, t_4]*:* At time t_3, i_{Cr} decreases to equal i_{Lm}, resulting in no flow of current through the ideal transformer. Thus, Q_5 and Q_8 carried by the synchronous rectification (SR) turn OFF under ZCS conditions. The ideal transformer is equivalent to an open circuit, as shown in the Fig. 4(d). Moreover, C_r and L_m form a series resonant structure, i.e., $i_{Cr} = i_{Lm}$ until the next half of the switching cycle, starting with the turning OFF of Q_2 and Q_3.

Similar to the LLC converter, when the switching frequency is larger than the resonant frequency, the converter cannot achieve ZCS.

B. Reverse Mode

The reverse energy transfer process is different from the forward mode. When f_s is lower than f_r, there are four modes in half cycle.

Stage 1 [t_0, t_1]*:* at time t_0, Q_6 and Q_7 turn OFF. The current through L_r charges C_{Q6} and C_{Q7}, while C_{Q5} and C_{Q8} discharges. At the end of this process, *vds*5,8 reaches the input voltage, and C_{Q5} and C_{Q8} discharge to zero. Given that the value of the parasitic capacitance is smaller than the value of the resonant capacitor C_r, this period is relatively short with respect to the total switching period. Moreover, i_{Cr} decreases rapidly under the action of resonance, forcing a portion of i_{La} to flow through Q_2 and Q_3. During this stage, i_{Cr} is lower than i_{Lm} in this mode. The equivalent circuit of this stage is shown in Fig. 5(a).

Stage 2 [t_1, t_2]*:* at time t_1, the body diode of Q_5 and Q_8 turns on and feeds back into the input source, thus creating conditions for ZVS switching. The equivalent circuit of this stage is shown in Fig. 5(b). The current of L_a decreases at a rate of $-V_2 \ / \ L_a$.

Stage 3 [t_2, t_3]*:* At time t_2, Q_5 and Q_8 conducting under ZVS conditions. Moreover, L_r, C_r, and L_m play an important role in the resonance. The current of L_r decreases to zero, and then increases in the negative polarity. The i_{Cr} decreases in a sinusoidal manner, and a portion of i_{Cr} flows into the output port through Q_2 and Q_3. The current of L_a reduces to zero at the same rate as that in the previous stage and increases in the reverse direction. The next stage begins when $i_{Cr} = iL_a$, as shown in Fig. 5(c).

Stage 4 [t_3, t_4]*:* at time t_3, i_{Cr} is equal to iL_a, and the current through Q_2 and Q_3 decreases to zero, thus realizing ZCS. Moreover, L_a participates in the resonance with the primary side during this stage.

The current of L_a increases in the negative polarity, thus making ZVS easier to achieve. As shown in Fig. 5(d), during this stage, no energy is transferred from the input to output. The first-half switching period ends at time *t*4, when *Q*1 and *Q*4 turn on under the ZVS conditions, and the converter enters the next half of the switching cycle.

In the reverse mode, when the switching frequency is greater than the resonant frequency, the ZCS condition is lost, and the switching loss is increased.

As can be seen from the analysis, the auxiliary inductor L_a accelerates the charging and discharging process of the parasitic capacitance, and then contributes to the realization of ZVS over a significantly short period of the dead time in the forward mode. At other times, L_a is clamped by the input voltage V_1 and the circuit is the same as the Type-11 LLC BRC; thus, the proposed LCLL BDC inherits the same soft-switching features as the Type-11 LLC tanks with a wide operating voltage range. In the reverse mode, L_a changes the waveform of the output current flowing to the V_1 port. At the same time, L_a accelerates the charge and discharge processes of the parasitic capacitance of the primary switches, which is beneficial to the realization of ZVS. When the switching frequency is greater than the resonant frequency, the forward mode and the reverse mode lose the ZCS characteristic.

III. Steady-State Model

A. Equivalent Model and Voltage Gain

The equivalent circuit for the forward mode is shown in Fig. 6(a), where R_{eq2} is the equivalent load resistance and L_{r1}

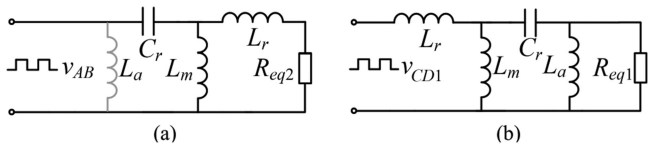

Fig. 6. Equivalent circuits with fundamental component assumption. (a) Forward mode. (b) Reverse mode.

is the equivalent resonant inductor of L_r. The current of the auxiliary inductor L_a does not transmit to the output; thus, it does not play a role in the resonance during the transmission. Thus, the auxiliary inductor L_a can be neglected in the calculation of the forward voltage gain. It should be noted that in reverse mode, the auxiliary inductor L_a and load are connected in parallel, as shown in Fig. 6(b). In Fig. 6(b), v_{CD1} represents the equivalent values referred to the primary side.

If the transformer turns ratio is n, the following is true:

$$L_r = n^2 \cdot L_{r1} \tag{1}$$

B. Voltage Gain for Forward Mode and Reserve Mode

The quasi-square voltages across the two bridges can be expressed as (2) and (3), where σ is the phase angle between the voltage square v_{AB} and v_{CD}

$$v_{\mathrm{AB}}(t) = \frac{4}{\pi} V_1 \sum_{n=1,3,5\ldots} \frac{1}{n} \sin(2\pi n f_s t) \tag{2}$$

$$v_{\mathrm{CD}}(t) = \frac{4}{\pi} V_{\mathrm{o}} \sum_{n=1,3,5\ldots} \frac{1}{n} \sin(2\pi n f_s t - \sigma). \tag{3}$$

The voltage gain can be obtained by the approach of the fundamental mode approximation (FMA) [37], [38]. The parameters v_{AB} and v_{CD} can then be represented by its fundamental sinusoidal component

$$v_{\mathrm{AB\cdot FHA}}(t) = \frac{4}{\pi} V_{\mathrm{in}} \sin(2\pi f_s t) \tag{4}$$

$$v_{\mathrm{CD\cdot FHA}}(t) = \frac{4}{\pi} V_o \sin(2\pi n f_s t - \sigma). \tag{5}$$

Hence, the equations of the dc gain for forward mode and reverse mode can be expressed as follows:

$$G_f = \frac{n \cdot V_2}{V_1} = \frac{A_f // (j\omega \cdot L_m)}{A_f // (j\omega \cdot L_m) + \frac{1}{j\omega \cdot C_r}} \cdot \frac{R_{\mathrm{eq2}}}{A_f} \tag{6}$$

$$G_r = \frac{A_r // (j\omega \cdot L_m)}{A_r // (j\omega \cdot L_m) + j\omega \cdot L_r} \cdot \frac{R_{\mathrm{eq1}} // j\omega \cdot L_2}{A_r} \tag{7}$$

where

$$R_{\mathrm{eq2}} = R_2 \cdot 8n^2/\pi^2 R_{\mathrm{eq1}} = R_1 \cdot 8/\pi^2 A_f = R_{\mathrm{eq2}} + j\omega \cdot L_r A_r = R_{\mathrm{eq1}} // j\omega \cdot L_2 + 1/j\omega \cdot C_r.$$

To simplify the expression of the voltage gain, four additional variables are required: the normalized frequency x, quality factor Q, and inductance ratio k_1 and k_2. These parameters are defined below. Moreover, k_1 is the ratio of the magnetizing inductor to the resonant inductor, and k_2 is the ratio of the auxiliary inductor to the resonant inductor

$$x = \frac{f_s}{f_r} \tag{8}$$

$$Q_i = \frac{\sqrt{\frac{L_r}{C_r}}}{R_{\mathrm{eq}i}} \tag{9}$$

$$k_1 = \frac{L_m}{L_r} \tag{10}$$

$$k_2 = \frac{L_a}{L_r}. \tag{11}$$

For the forward mode, it was reported in [6] that the resonance frequency of the T-11 LLC is the same as that of the T-4 LLC under the same parameters of resonant elements. Hence, the relationship between the resonance frequency f_{rf} of the LCLL and f_{rT-4} of the T-4 LLC is given by

$$f_{rf} = \frac{1}{2\pi \cdot \sqrt{\frac{L_m \cdot L_r}{L_m + L_r} \cdot C_r}} = \sqrt{\frac{k_1 + 1}{k_1}} \cdot f_{rT-4}. \tag{12}$$

Expression (6) can be rewritten with respect to x, Q, k_1, and $f_{rf;}$ and the simplified voltage gain is given by

$$G_f(x, Q, k_1) = \frac{1}{\sqrt{\left[1 - \frac{1}{(1+k_1)x^2}\right]^2 + \frac{Q^2(1+k_1)}{k_1}(x - \frac{1}{x})^2}}. \tag{13}$$

According to the forward voltage gain formula, when the normalized frequency x is 1, the voltage gain is independent of the quality factor Q (or load R), and it is only dependent on k_1. In addition, the voltage gain at the resonance frequency changes from its value of 1. This is because the resonant frequencies of T-11 LLC and T-4 LLC are different, thus resulting in different voltage gains of the two types of LLC at the normalized frequency $x = 1$.

Based on the forward voltage gain formula, the forward voltage gain characteristics of the proposed topology were plotted using PTC Mathcad, as shown in Fig. 7. Fig. 7(a) presents the relationship between the quality factor Q and voltage gain G. With a decrease in Q, G increases, and the curve shifts to the left. Fig. 7(b) presents the relationship between k_1 and the voltage gain G. With a decrease in k_1, the gain G increases, and the curve shifts to the right.

There are two resonance frequencies in the reverse mode. The first is dependent on L_m, C_r, and L_r. The second is dependent on L_m, C_r, L_a, and the load condition. With an increase in the load, the resonant frequency increases. The resonant frequencies of reserve mode are as follows:

$$f_{rr} = \sqrt{\frac{k_1 + 1}{k_1}} \cdot f_{rT-4} = f_{rf} \tag{14}$$

$$f_{rr2} = \sqrt{\frac{k_1 + 1}{k_1 + k_2 + k_1 \cdot k_2}} \tag{15}$$

where $f_{rT-4} = 1/\sqrt{L_r \cdot C_r}$.

The main resonant frequency of the reserve mode is equal to that of the forward mode, which can be expressed by (14).

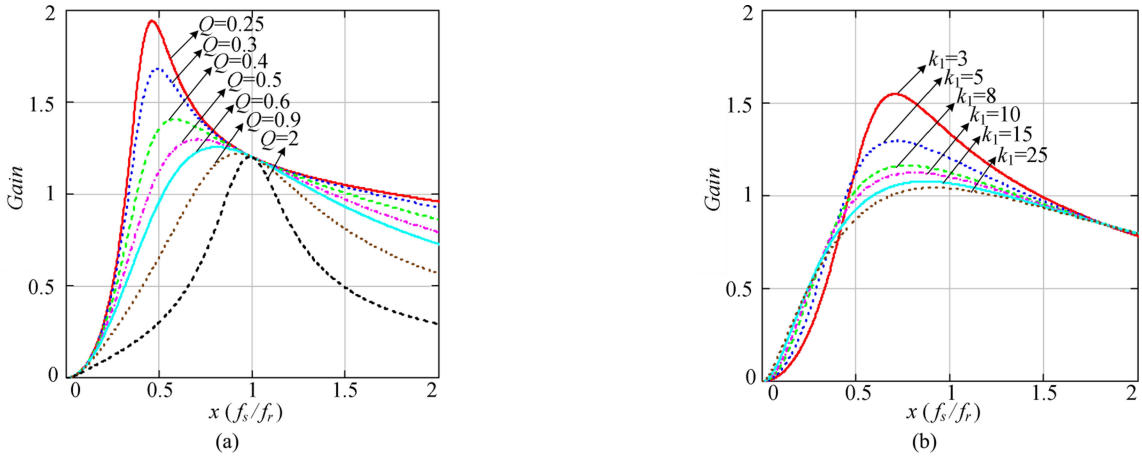

Fig. 7. Parameter sweep in scale under forward modes. (a) Sweep in scale of Q ($k_1 = 5$). (b) Sweep in scale of k_1 ($Q = 0.5$).

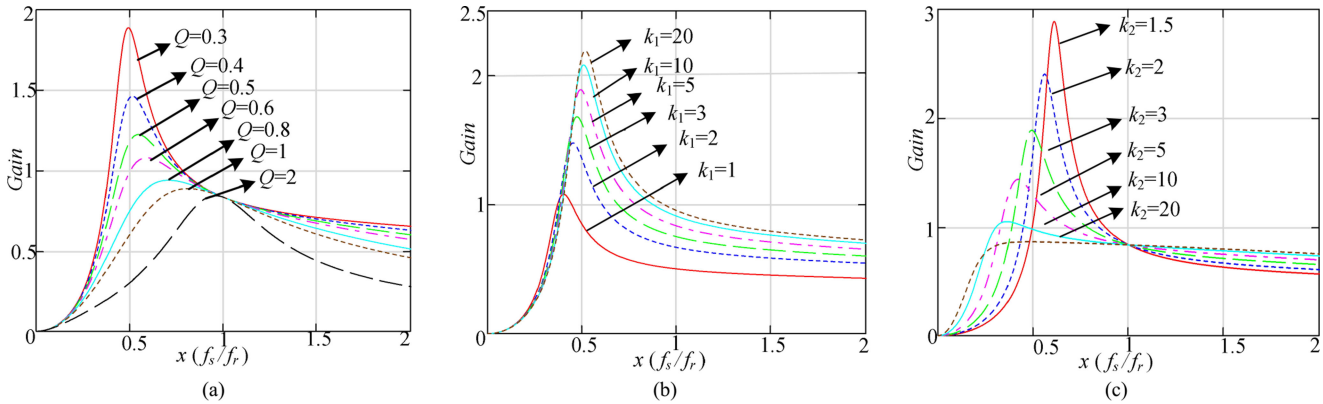

Fig. 8. Parameter sweep in scale under reverse modes. (a) Sweep in scale of Q. (b) Sweep in scale of k_1. (c) Sweep in scale of k_2.

Thus, the resonant frequency can be expressed as f_r for both modes

$$G_r(x, Q, k_1, k_2) = \frac{1}{\sqrt{\left[1 + \frac{1}{k_1} + \frac{x^2-1}{k_2 x^2}\right]^2 + \frac{Q^2(1+k_1)}{k_1}\left(x - \frac{1}{x}\right)^2}}. \tag{16}$$

When the normalized frequency $x = 1$, the voltage gain is independent of the quality factor Q (or load R) and k_2, and it is only dependent k_1.

Based on the reverse voltage gain formula, the gain characteristic curve was plotted using PTC Mathcad. Reverse voltage gain characteristics are shown in Fig. 8. Fig. 8(a) presents the relationship between the quality factor Q and the voltage gain G. With a decrease in Q, the gain G increases, and the curve shifts to the left. Fig. 8(b) presents the relationship between k_1 and G. It was found that with an increase in k_1, G increases, and the curve shifts to the left. Fig. 8(c) presents the relationship between k_2 and G. Bigger k_2 is conductive to a steeper G, and the curve shifts to the right. Fig. 9 presents the contrast between the voltage gain curve of the bidirectional LLC topology and the proposed voltage gain curve of the LCLL. The gain characteristic is the same as that of the T-4 tank in the reverse mode, which is suitable for wide output voltage ranges. Besides, The LCLL

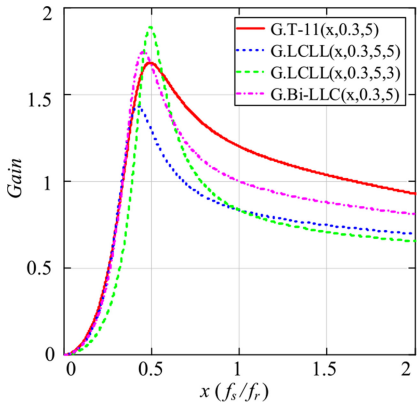

Fig. 9. Comparison of LCLL and bidirectional LLC reverse transmission characteristic, and theT-11 LLC forward transmission characteristic.

with an auxiliary inductor has a wider voltage regulation range than the T-11 resonator with suitable parameters. It can be seen that a higher gain curve gradient than that of the LLCL can be realized by selecting an appropriate k_2 value, and then a wider port-voltage range can be obtained.

As verified by the forward and reverse voltage gain curves, the proposed converter can achieve step-up and step-down under

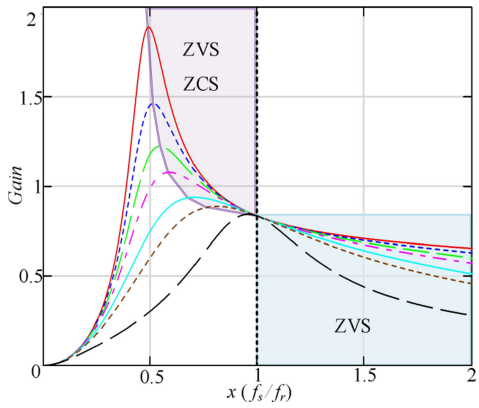

Fig. 10. Voltage gain versus the operating switching frequency curves under different load conditions.

forward and reverse operating conditions, which is in accordance with the characteristics of a wide voltage range output. This overcomes the drawbacks of T-4 LLC and T-11 LLC, in that they can only step-down when operated in the reverse mode. At the same time, the additional element L_a is added to simplify the parameter design; when compared with CLLC, which has two peaks. Only one peak value was observed in the forward and reverse voltage gain curves of the topology, and PFM control is simple, which is critical for further parameter design.

C. Soft Switching and Design Proceduce for the LCLL Resonant Tank

According to the voltage gain characteristic curve presents above, it can be assumed that the switching frequency of the proposed converter is $f_{\max}$ at the peak value and f_r at the normalized frequency $x = 1$. These two frequencies divide the gain curve into three parts. As shown in Fig. 10, when f_s is less than $f_{\max}$, the ZVS and ZCS characteristics are lost at the inverter side; and when $f_{\max} < f_s < f_r$, the switches on the inverter side are in ZVS state, and the switches on the rectifier side are in ZCS state. When $f_r = f_s$, the rectifier side switches are in the critical ZCS state. When $f_r < f_s$, the inverter side switches are in the ZVS state, and the rectifier side switches will lose their ZCS characteristics. To achieve a high efficiency, it is necessary to control the switching frequency between $f_{\max}$ and f_r.

As mentioned previously, the voltage gain of T-11 LLC is not 1 when the switches are operated at the resonant frequency, and it varies in accordance with variations in the value of k_1. In particular, with a decrease in k_1, the voltage gain increases, and the voltage gain curve shifts to the right. The slope of the curve increases, which increases the complexity of the control strategy. Conversely, with an increase in the voltage gain, the gain curve shifts to left, thus simplifying the control strategy.

There is only one peak point in the voltage gain curve of the proposed converter. Moreover, when the switch frequency is greater than the peak frequency, the curve of voltage gain monotonically decreases. In this article, $k_1 = 4.5$ was selected as the trade-off value, to obtain a significantly wider output voltage and simpler control strategy.

Based on the conclusions from the previous analysis the following resonance frequency calculation expression and voltage gain expression of T-11 LLC can be obtained by (6), (12), and (17)

$$G_f = \frac{n \cdot v_2}{v_1} \tag{17}$$

If the component parameters are the same as those of the T-4 LLC, the resonant frequency $f_{rT-4} = 100$ kHz and the $f_r = 110$ kHz, as determined using Expression (6).

It can be concluded from Expression (12) that Q is independent of R when the switching frequency is equal to the resonant frequency. At the same time, to achieve a higher transmission efficiency, the rated operating point of the converter can be set to operate at the resonant frequency. Hence, based on Expression (17), the transformer ratio is $n = 1.2$ when $G_f = 1.2$.

To realize wider forward and reserve output voltage ranges, the selection of a suitable set of parameters (L_m, L_r, C_r) values is required. In the proposed converter, the dead time between the upper and lower side switches is set as 200 ns, and the shunt capacitance on the inverter side is set as 250 pF. To ensure that the inverter side switch can achieve ZVS, the range of magnetizing inductance values should satisfy (18) [8]. In addition, L_m, L_r, and C_r should satisfy (19) and (20)

$$L_m \leq \frac{T \cdot t_{\text{dead}}}{16 \cdot C_{\text{oss}}} \tag{18}$$

$$L_m = k_1 L_r \tag{19}$$

$$C_r = \frac{1}{L_r \cdot (2\pi \cdot f_r)^2} \tag{20}$$

The design process is simplified to the following steps without considering the parasitic components of the transformer [39].

Step 1: Select an appropriate value of L_m

The selection of L_m has a direct influence on the efficiency of the converter (transformer) and the output voltage range. if the L_m is small, the I_m of the transformer increases. With an increase in L_m, there is a decrease in the I_{RMS} of the current flowing through the switch, thereby reducing switching losses. However, the output voltage range is limited, and the switching frequency range increases [40]. Therefore, the selection of L_m should be balanced between the transmission efficiency and output voltage range.

With the voltage output range $V_1 \in$[80 V, 120 V], the voltage gain range that be calculated from (16) is [0.96,1.44]. By changing the inductance value, a cluster of voltage gain curves can be obtained.

As can be seen Fig. 11(a), based on the output voltage range and switch frequency range, setting $L_m = 50$ μH, $L_r = 10.42$ μH, and $C_r = 300$ nF is appropriate to obtain the max gain (1.44). In particular, a 7.23 μH inductor is placed on the secondary side of the transformer, which is equivalent to the primary side inductance L_r.

Step 2: Choose the proper value of L_a

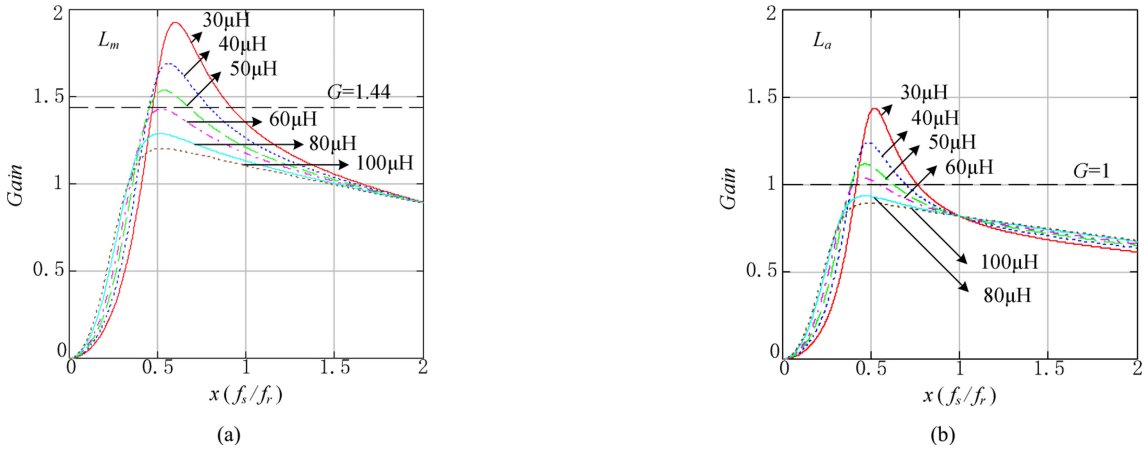

Fig. 11. Parameters sweep in scale. (a) Parameter sweep in scale of L_m under forward mode. (b) Parameter sweep in scale of L_a under reverse mode.

TABLE I
CURRENT AND VOLTAGE STRESS OF KEY COMPONENTS

	I_{Lmp}	I_{Lrp}	V_{Crp}	I_{Lap}
T-4	$\frac{n\cdot V_2}{2\cdot L_m\cdot f_s}$	$\frac{\sqrt{2}V_2}{8\cdot n\cdot R}\sqrt{\frac{2\cdot n^4\cdot R^2}{{L_m}^2\cdot {f_{rT-4}}^2}+8\pi^2}$	$n\cdot V_2+\frac{I_o}{4\cdot n\cdot C_r\cdot f_s}$	--
T-11	$\frac{V_2}{8\pi\cdot L_m\cdot R}\sqrt{\pi^6\cdot {L_{r1}}^2\cdot n^8+\frac{16\cdot R^2}{f_r^2}}$	$\frac{\pi^2\cdot V_2\cdot n^2}{8\cdot R}$	$\frac{G_f\cdot V_1\cdot\sqrt{\pi^6\cdot {L_2}^2\cdot {f_s}^2\cdot n^4+16\cdot R^2}}{16\pi^2\cdot C_1\cdot L_1\cdot R\cdot f_s}$	--
LCLL (forward)	$\frac{V_2}{8\pi\cdot L_m\cdot R}\sqrt{\pi^6\cdot {L_{r1}}^2\cdot n^8+\frac{16\cdot R^2}{f_r^2}}$	$\frac{\pi^2\cdot V_2\cdot n^2}{8\cdot R}$	$\frac{G_f\cdot V_1\cdot\sqrt{\pi^6\cdot {L_2}^2\cdot {f_s}^2\cdot n^4+16\cdot R^2}}{16\pi^2\cdot C_1\cdot L_1\cdot R\cdot f_s}$	$\frac{V_1}{4\cdot L_a\cdot f_s}$
DAB	--	$\frac{2\cdot n\cdot V_2\cdot D_\varphi-n\cdot V_2+V_1}{4\cdot L_r\cdot f_s}$	--	--

As shown in Fig. 11(b), a set of reverse voltage gain curves can be obtained by using the same method calculated according to (14).

With an increase in L_a, the transmission efficiency of the converter increases, and the voltage gain decreases. The expected output voltage is [80, 120]; thus, the voltage gain is [0.667, 1]. Therefore, to obtain a higher efficiency and realize the expected output voltage range, a larger value of L_a is preferable. Hence, $L_a = 40$ μH was selected as an appropriate value, which can yield the expect output voltage range and an improved switch frequency range.

These parameters were compared on the simulation platform shown in Fig. 10(b). With an increase in L_a, the gain curve shifts to the left, the resonance frequency decreases, and the peak value of the voltage gain curve decreases. This effect is gradually mitigated in accordance with an increase in resistance.

The voltage and current stresses of key devices are given in Table I.

IV. EXPERIMENTAL RESULTS

To validate the converter design, a 1000-W bidirectional resonant converter was developed in the laboratory. Given that the UCD3138 (Texas Instruments, Dallas, Texas, United States of America) is very suitable for the development of a digital control experimental platform in this experiment, a UCD3138 was used to carry out PFM control, for the verification of the output features of the forward mode and the reverse mode. To synthesize the above analysis, the parameters of the entire converter are shown in the following table. The core of the transformer is 3C95EE55, and the core of the auxiliary inductor is 3C95EE35. For full load, the maximum frequency $f_{s\max}$ is set as 120 kHz due to the switching loss. Moreover, the minimum frequency $f_{s\min}$ is limited to 65 kHz, keeping away from the peak gain.

The physical diagram of the prototype is shown in Fig. 12. Moreover, the power system combined by the dynamic dc power supply Keysight N7976A and its power dissipater unit

TABLE II
COMPONENTS AND PARAMETER

Parameter	Value	Unit
Transformer ratio n	1.2	-
Magnetizing inductance L_m	50.2	μH
the leakage inductance of the transformer L_l	1.5	μH
Resonant inductor L_r (L_{r1})	9.9 (6.9)	μH
Resonant capacitor C_r	300	nF
Auxiliary inductance L_a	39.9	μH
Ideal resonant frequency f_{ri}	95	kHz
Actual resonant frequency f_r	92	kHz
Switches Q_1 - Q_8(MOSFET)	IRFP90N20D	-

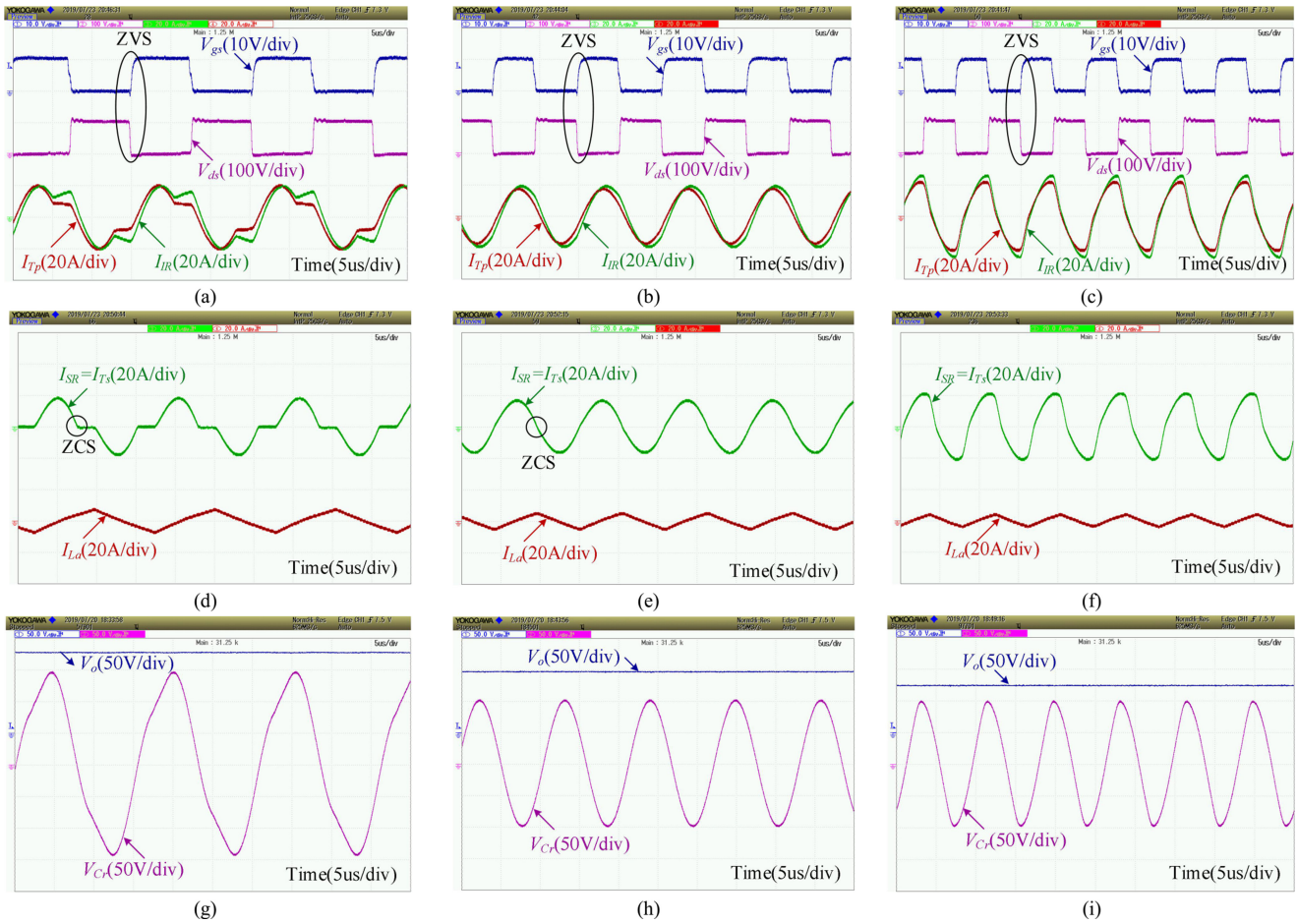

Fig. 12. Experimental waveforms for the forward mode. (a) v_{gs} and v_{ds} of Q_1, i_{IR}, i_{Tp} for $f_s < f_r$. (b) $v\,v_{gs}$ and v_{ds} of Q_1, i_{IR}, i_{Tp} for $f_s = f_r$. (c) v_{gs} and v_{ds} of Q_1, i_{IR}, i_{Tp} for $f_s > f_r$. (d) i_{SR} which equals to i_{Ts} and i_{La} for $f_s < f_r$. (e) i_{SR} which equals to i_{Ts} and i_{La} for $f_s = f_r$. (f) i_{SR} which equals to i_{Ts} and i_{La} for $f_s > f_r$. (g) v_{cr} and v_o, when v_o is 129 V for $f_s < f_r$. (h) v_{cr} and v_o, when v_o is 100 V for $f_s = f_r$. (i) v_{cr} and v_o, when v_o is 77 V for $f_s > f_r$.

N7909A operated as the energy storage device. The oscilloscope is YOKOGAWA DLM 2024.

A. *Topology Operation Verification*

The operation waveforms are shown in Fig. 12. The following experiment was carried out at a constant power (CP) output load equal to 1000 W. The current flowing through the switches at the inverter side is I_{IR}, and that of in the SR side is I_{SR}. The transformer current of the primary side is I_{Tp}, and that of the secondary side is I_{Ts}.

In the forward mode, the controller commands the MOSFETs operating at the desired switching frequency, under approximately 50% duty for each bridge. Fig. 12(a)–(c) present the ZVS feature of the switches, irrespective of the switch frequency, for $f_s < f_r$, f_s f_r, or $f_s > f_r$. The maximum output voltage is 129 V, whereas the switching frequency is near 65 kHz in Fig. 12(a). With the arrival of the drive signal of Q_1, the current I_{IR} is negative, which indicates that the capacitor parallel with the MOS discharged to zero and the body diode is ON. This satisfies the ZVS condition. This process demonstrates that although the auxiliary inductor increases the power reflow; this current, as shown in Fig. 12(d), helps to achieve the ZVS of the switches. When the output voltage is equal to the input voltage, the switching frequency is equal to the resonant frequency. As shown in Fig. 12(b), the resonant frequency is approximately 92 kHz, and the current waveform that flows into the transformer is approximately sinusoidal. The ZVS process of Fig. 12(c) is similar to Fig. 12(a).

Fig. 12(d)–(f) present the waveforms of the secondary side current of the transformer and the current of L_a. The turn-off feature of the SR switches varies with frequency. When $f_s < f_r$, the current of the switches on the secondary side are discontinuous, thus realizing ZCS. The main reason is that the i_{Cr} and i_{Lm} are equal before switch-state changes between different bridges. The primary side does not transmit energy to the secondary side; thus, the current of secondary side is discontinuous. When $f_s = f_r$, the current of the SR switches is in critical continuity. The switches at the primary side can realize ZVS, and the switches at the secondary side can realize ZCS. However, when $f_s > f_r$, the excitation current can never be equal to the resonant current; thus, the output current of the switches at the secondary side is continuous, and ZCS cannot be realized.

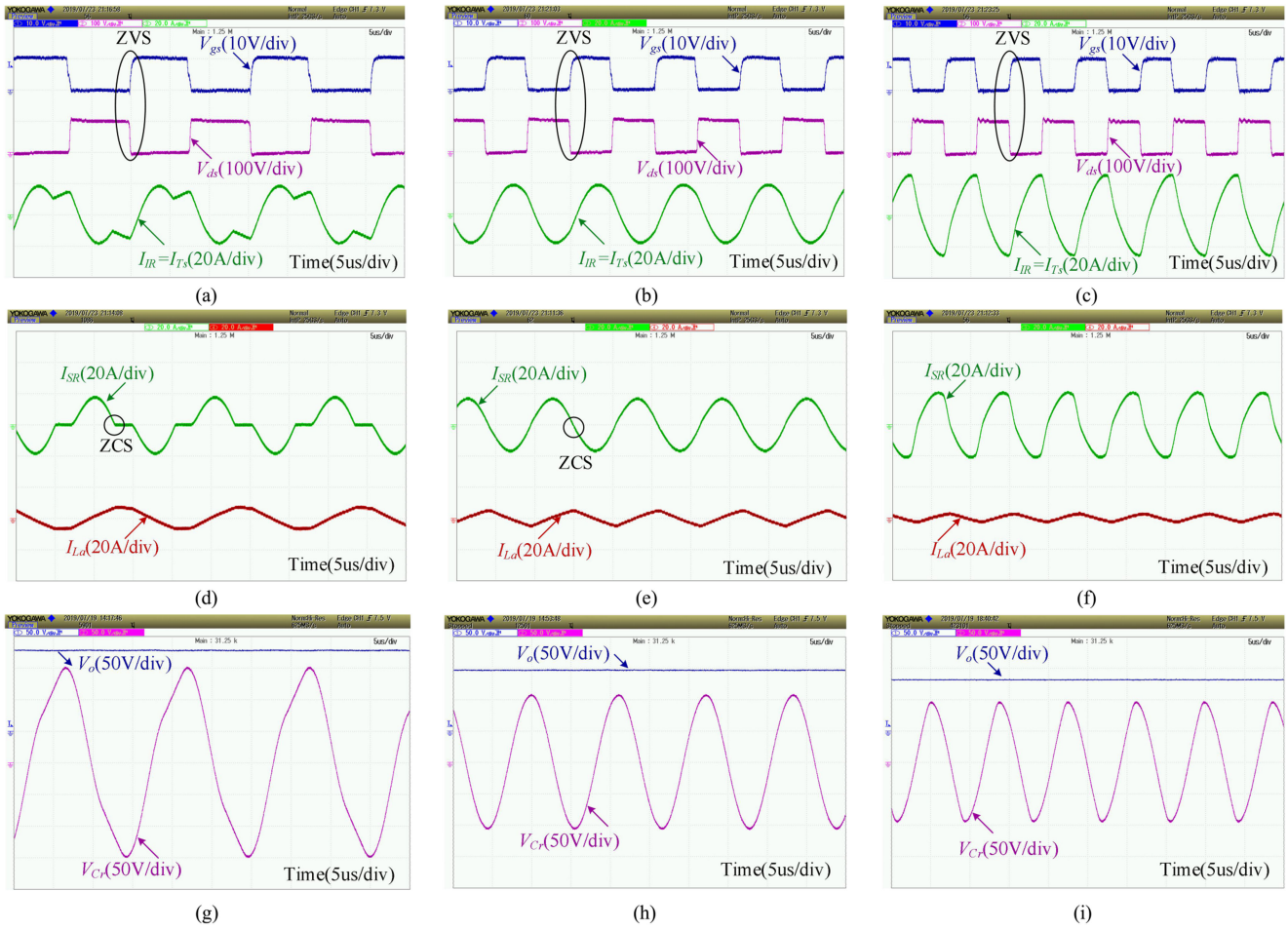

Fig. 13. Experimental waveforms for the reverse mode: (a) v_{gs} and v_{ds} of Q_6 and i_{IR}, which equals to i_{Ts} for $f_s < f_r$. (b) v_{gs} and v_{ds} of Q_6 and i_{IR}, which equals to i_{Ts} for $f_s = f_r$. (c) v_{gs} and v_{ds} of Q_6 and i_{IR}, which equals to i_{Ts} for $f_s > f_r$. (d) i_{SR} and i_{La} for $f_s < f_r$. (e) i_{SR} and i_{La} for $f_s = f_r$. (f) i_{SR} and i_{La} $f_s > f_r$. (g) v_{cr} and v_o, when v_o is 130 V for $f_s < f_r$. (h) v_{cr} and v_o, when v_o is 100 V for $f_s = f_r$. (i) v_{cr} and v_o, when v_o is 73 V for $f_s > f_r$.

From the experimental waveform of the output voltage and resonant capacitor voltage given in Fig. 12(g)–(i), it can be seen that step-up and step-down can be achieved by adjusting the switching frequency. The output voltage reaches 129 V, and the resonant capacitor voltage is an approximate sinusoidal alternating current (AC) voltage with an amplitude of 300 V. When $f_s = f_r$, the output voltage at the resonant frequency is theoretically rated 100 V, and the resonant capacitor voltage is a sinusoidal AC waveform with an amplitude of 110 V. When $f_s > f_r$, the minimum output voltage is 77 V, and the amplitude of the resonant capacitor voltage is 110 V. The experimental results verify that the proposed topology can achieve wide voltage output in the forward mode.

In the reserve mode, the operation waveforms of full load under outputs ranging from 73–130 V are shown in Fig. 13(a)–(i). Fig. 13(a)–(c) present the ZVS feature of Q_6, where it can be observed that I_{IR} is negative before the arrival of its driving signal. Fig. 13(d) and (f) present the current waveforms of the switches at the output side, which demonstrates the implementation of ZCS. The auxiliary inductor L_a in the reverse mode plays a similar role to the primary magnetizing inductor in the forward mode.

Based on the experimental waveforms of the output voltage and resonant capacitor voltage presented in Fig. 13 (i) and (j); when $f_s < f_r$, step-up is achieved by reducing the switching frequency.

The output voltage range of the reverse mode is close to the forward mode. The experimental results verify that the proposed topology can achieve a wide voltage output in the reverse mode.

The experimental results for the step response test of the load are shown in Fig. 14 for the forward mode and reverse mode. The output load is stepped from 1 to 5 A, then to 10 A. As shown in Fig. 14(a), during the process, the output voltage stabilizes at 100 V by the closed-loop compensation adjustment. The experimental results reveal that the designed forward compensation can stabilize the output voltage by 100 V without significant overshoot. Similarly, Fig. 14(b) presents the output voltage and output current in the reverse mode under the step load.

B. *Numerical Model Verification*

Fig. 15 shows the voltage gain comparison of the calculated results based on FMA, the simulated results based on PSIM and the measured results based on experiments. All the simulations

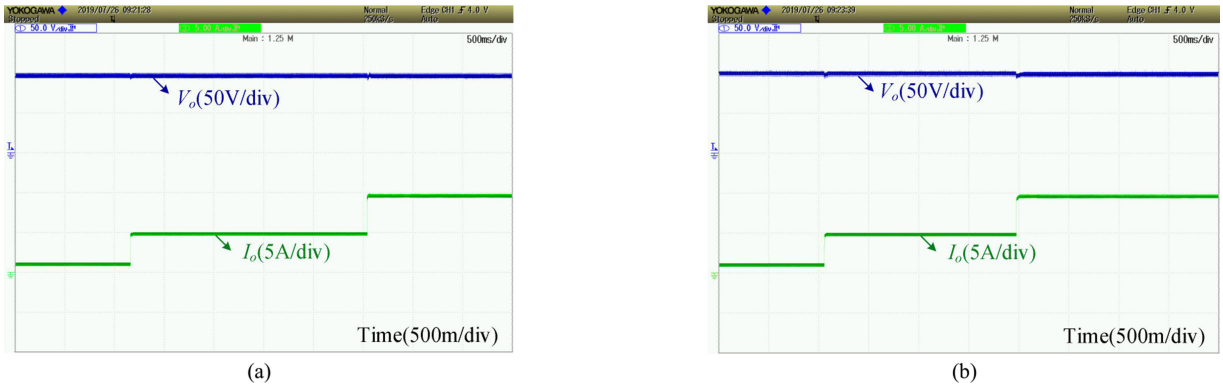

Fig. 14. Response for step load. (a) For the forward mode. (b) For the reverse mode.

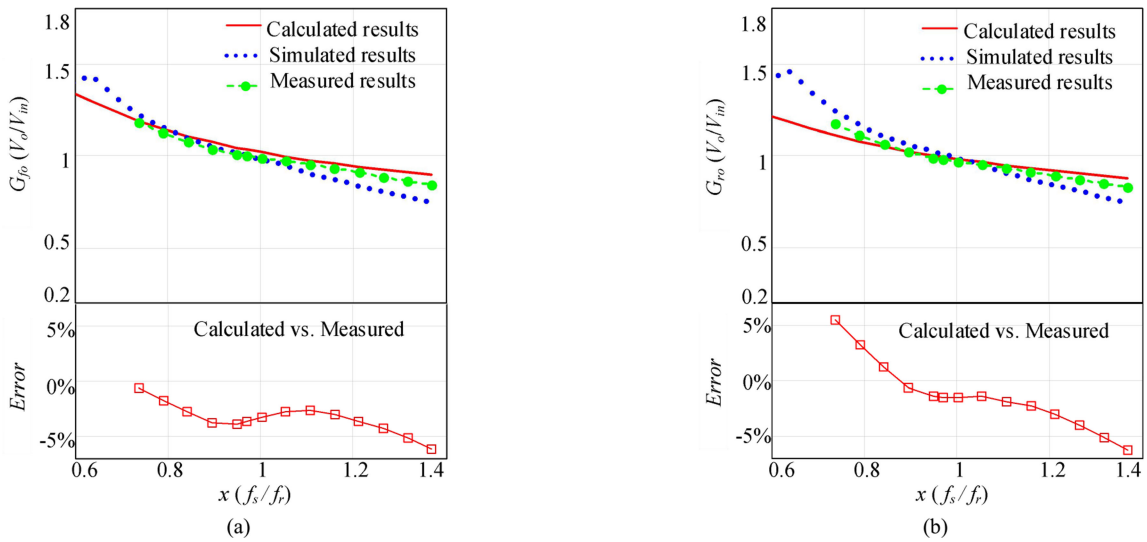

Fig. 15. Calculated, simulated and measured output voltage gain, and errors between calculated and simulated results. (a) Forward mode. (b) Reverse mode.

and experiments are taken under the condition of the input voltage is 100 V and the load is 10 Ω. It can be seen that the slope of voltage gain of the simulated result based on the time domain analysis is larger than that of the calculated result around the peak gain. The error around resonant frequency between calculated results and measured results hardly changes. The errors between measured results and calculated results vary from -0.8% to -6.7% for the forward, and range from -6.1% to 5.3% for the reverse mode. The difference of voltage gain between the measured one and the calculated one is mainly caused by the assumption in calculating and the voltage drop on the power devices.

C. Efficiency Comparison

In the LCLL converter proposed in this article, the value of L_a needs to be selected in a compromise. The smaller L_a, the steeper the gain curve can be obtained, while the losses of the auxiliary inductor will also increase. The reason for increasing L_a is to reduce the losses, but this obviously increases the volume and weight of the magnetic devices. Table III gives a comparison of the two parameters. Case 1 and case 2 have similar k_1 values. The two sets of parameters use the same magnetic cores, but the parameters with larger inductance value are more efficient and the weight is also heavier. Under the two parameters of the experiment, case 1 with higher inductance value has higher power density.

Table III also shows the comparison of LCLL with T-4 LLC (bidirectional LLC), T-11 LLC, and DAB. DAB controlled by SPS method has a full-load efficiency similar to that of the proposed LCLL, but is less efficient under light-load conditions. Compared with bidirectional LLC, the proposed LCLL is more efficient. This is because in order to achieve a wide range, the rated operating point is no longer at the resonance point. Compared with T-11 LLC, LCLL adds auxiliary inductance L_a that improves the reverse gain characteristic of T-11, so the loss increases and the efficiency is lower.

The transmission efficiency of proposed LCLL, bidirectional LLC, T-11 LLC, and DAB for different voltage gain conditions under full load is recorded and shown in Fig. 16, as the input voltage was set as 100 V. The experiments have shown that the full load efficiency of DAB is better than the proposed LCLL when in the step-down range. But in the boost interval, the efficiency of DAB is lower than LCLL. This is because as the gain

TABLE III
KEY CIRCUIT PARAMETERS IN DIFFERENT CASES

	L_r/μH	L_m/μH	C_r/nF	L_a/μH	n	f_r or f_s /kHz	η@100V, 10R		Number of magnetic devices
LCLL case 1	9.9	50.2	300	39.9	12:10	92	forward reverse	95.94% 95.61%	3
LCLL case 2	4.58	29.4	470	28μH	12:10	100	forward reverse	94.1% 93.83%	3
T-4 LLC	5.0	50.2	620	--	12:10	87	--	94.22%	2
T-11 LLC	9.9	50.2	300	--	12:10	92	--	96.57%	2
DAB SPS	5.5	512	--	--	10:11	100	forward reverse	95.01% 95.57%	2

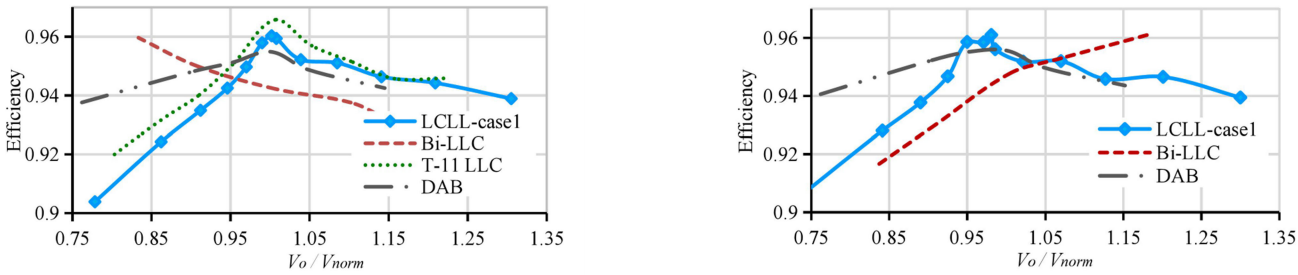

Fig. 16. Measured efficiency at different output voltage. (a) For the forward mode. (b) For the reverse mode.

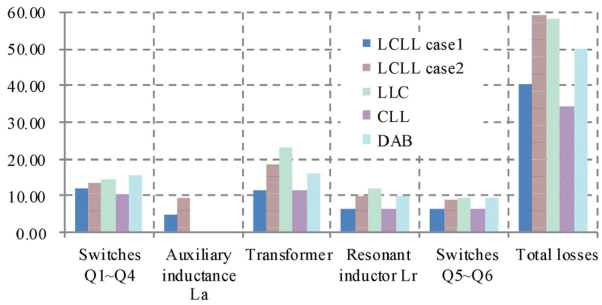

Fig. 17. Loss breakdown for the forward mode

increases, the switching frequency of the LCLL decreases, and the switch-off loss is significantly reduced. For the bidirectional LLC converter, when the forward voltage gain is close to 0.8, and when the reverse voltage gain is close to 1.2, it operates at the resonant frequency. And the converter efficiency is significantly higher than DAB and LCLL. However, it decreases significantly due to the continuous increase of the switching frequency.

Fig. 17 shows the loss analysis. The efficiency curve under forward conditions was obtained, as shown in Fig. 16(a). The efficiency is the highest and reaches 96.0% when $f_s = f_r$. Moreover, the efficiency curve in the reverse mode was obtained, as shown in Fig. 16(b). The efficiency is the highest and reaches 96.1% when $f_s = f_r$. Operated in the ZVS and ZCS region that correspon to $f_s < f_r$, in which the voltage gain is larger than 1, the efficiency is higher than the ZCS region without ZVS. Due to the realization of ZVS and ZCS, the efficiency loss of the converter is mainly due to the core loss and copper loss of the magnetic device. The converter also has the problem of circulating energy. The circulating energy is defined as the energy transmitted back to input source in each switching cycle. Based on the waveforms shown in Fig. 12(a) and (b), the circulating energy at an input voltage of 129 V is larger than that at 100 V, which increases the conduction loss. Especially for the forward transmission mode, L_a increases the circulating current. It is therefore necessary to rationally configure and optimize the efficiency according to the practical application.

V. CONCLUSION

This article proposes a bidirectional LCLL resonant topology features wide voltage range. An auxiliary inductor is added to improve the voltage gain of reverse mode, so that the disadvantage of T-11 LLC resonant tank that the voltage can not be boosted under the reverse condition is solved. The formula of voltage gain for the novel resonant tank is given, and the parameters are analyzed by normalization. However, the auxiliary inductor increases power loss. The calculation results show that, by adjusting the parameters of the auxiliary inductor with the same proportion of resonant parameters, the gain curve can be steeper than that of LLCL resonant topology. At the same time, the ZVS for the inverting switches and ZCS for the rectifier switches can be realized regardless of the direction of the power flows. The operation principles and design procedure of the proposed converter have been analyzed and depicted. The experimental results from 1 kW prototype verify the theoretical analysis. Efficiency above 96% was achieved at full load condition. The experiment is controlled by PFM. The experimental results show that the proposed converter can realize the wide output range and soft switching characteristic by adjusting the switching frequency in both forward and reverse mode, which is quite attractive for energy storage system applications.

REFERENCES

[1] G. Tibola and J. L. Duarte, "Isolated bidirectional DC-DC converter for interfacing local storage in two-phase DC grids," in *Proc. IEEE 8th Int. Symp. Power Electron. Distrib. Gener. Syst.*, 2017, pp. 1–8.

[2] H. Zhu, D. Zhang, H. S. Athab, B. Wu, and Y. Gu, "PV isolated three-port converter and energy-balancing control method for PV-battery power supply applications," *IEEE Trans. Ind. Electron.*,vol. 62, no. 6, pp. 3595–3606, Jun. 2015.

[3] B. Zhao, Q. Song, W. Liu, and Y. Sun, "Overview of dual-active-bridge isolated bidirectional DC–DC converter for high-frequency-link power-conversion system," *IEEE Trans. Power Electron.*, vol. 29, no. 8, pp. 4091–4106, Aug. 2014..

[4] H. Bai and C. Mi, "Eliminate reactive power and increase system efficiency of isolated bidirectional dual-active-bridge dc–dc converters using novel dual-phase-shift control," *IEEE Trans. Power Electron.*, vol. 23, no. 6, pp. 2905–2914, Nov. 2008.

[5] H. Wen, W. Xiao, and B. Su, "Nonactive power loss minimization in a bidirectional isolated DC–DC converter for distributed power systems," *IEEE Trans. Ind. Electron.*, vol. 61, no. 12, pp. 6822–6831, Dec. 2014.

[6] C. Mi, H. Bai, C. Wang, and S. Gargies, "Operation, design and control of dual H-bridge-based isolated bidirectional dc-dc converter," *IET Power Electron.*, vol. 1, no. 4, pp. 507–517, Dec. 2008.

[7] B. Zhao, Q. Yu, and W. Sun, "Extended-phase-shift control of isolated bidirectional dc-dc converter for power distribution in microgrid," *IEEE Trans. Power Electron* ., vol. 27, no. 11, pp. 4667–4680, Nov. 2012.

[8] B. Zhao, Q. Song, and W. Liu, "Power characterization of isolated bidirectional dual-active-bridge dc-dc converter with dual-phase-shift control," *IEEE Trans. Power Electron.*, vol. 27, no. 9, pp. 4172–4176, Sep. 2012.

[9] D. Costinett, R. Zane, and D. Maksimovic, "Automatic voltage and dead time control for efficiency optimization in a Dual Active Bridge converter," in *Proc. 27th Annu. IEEE Appl. Power Electron. Conf. Expo.*, 2012, pp. 1104–1111.

[10] Q. Huang, K. Shi, X. Jia, C. Hu, and D. Xu, "A bi-directional resonant DC/DC converter with frequency tracking control," in *Proc. IEEE Energy Convers. Congr. Expo.*, 2014, pp. 4748–4754.

[11] T. Jiang, J. Zhang, X. Wu, K. Sheng, and Y. Wang, "A bidirectional LLC resonant converter with automatic forward and backward mode transition," *IEEE Trans. Power Electron.*, vol. 30, no. 2, pp. 757–770, Feb. 2015.

[12] J. Jung, H. Kim, M. Ryu, and J. Baek, "Design methodology of bidirectional CLLC resonant converter for high-frequency isolation of DC distribution systems," *IEEE Trans. Power Electron.*, vol. 28, no. 4, pp. 1741–1755, Apr. 2013.

[13] C. Wang, S. Zhang, Y. Wang, B. Chen, and J. Liu, "A 5-kW isolated high voltage conversion ratio bidirectional CLTC resonant DC–DC converter with wide gain range and high efficiency," *IEEE Trans. Power Electron.*, vol. 34, no. 1, pp. 340–355, Jan. 2019.

[14] H. Wu, K. Sun, Y. Li, and Y. Xing, "Fixed-frequency PWM-controlled bidirectional current-fed soft-switching series-resonant converter for energy storage applications," *IEEE Trans. Ind. Electron.*, vol. 64, no. 8, pp. 6190–6201, Aug. 2017.

[15] T. Jiang, J. Zhang, X. Wu, K. Sheng, and Y. Wang, "A bidirectional threelevel LLC resonant converter with PWAM control," *IEEE Trans. Power Electron.*, vol. 31, no. 3, pp. 2213–2225, Mar. 2016.

[16] Y. Shen, H. Wang, A. Al-Durra, Z. Qin, and F. Blaabjerg, "A bidirectional resonant dc-dc converter suitable for wide voltage gain range," *IEEE Trans. Power Electron.*, vol. 33, no. 4, pp. 2957–2975, Apr. 2018.

[17] T. LaBella, W. Yu, J. Lai, M. Senesky, and D. Anderson, "A bidirectional-switch-based wide-input range high-efficiency isolated resonant converter for photovoltaic applications," *IEEE Trans. Power Electron.*, vol. 29, no. 7, pp. 3473–3484, Jul. 2014.

[18] H. Hu, X. Fang, F. Chen, Z. J. Shen, and I. Batarseh, "A modified high-efficiency LLC converter with two transformers for wide input-voltage range applications," *IEEE Trans. Power Electron.*, vol. 28, no. 4, pp. 1946–1960, Apr. 2013.

[19] W. Sun, Y. Xing, H. Wu, and J. Ding, "Modified high-efficiency LLC converters with two split resonant branches for wide input-voltage range applications," *IEEE Trans. Power Electron.*, vol. 33, no. 9, pp. 7867–7879, Sep. 2018.

[20] Y. Shen, H. Wang, A. Al-Durra, Z. Qin, and F. Blaabjerg, "Double voltage rectification modulation for bidirectional dc/dc resonant converters for wide voltage range operations," *IEEE Trans. Power Electron.*, vol. 34, no. 7, pp. 6510–6521, Jul. 2019.

[21] B. Chen, P. Wang, Y. Wang, S. Zhang, L. Yang, and R. Ji, "A bidirectional CDT-LC resonant DC–DC converter with a wide voltage range," *IEEE Trans. Ind. Electron.*, vol. 67, no. 3, pp. 2009–2020, Mar. 2020.

[22] L. Corradini, D. Seltzer, D. Bloomquist, R. Zane, D. Maksimović, and B. Jacobson, "Minimum current operation of bidirectional dual-bridge series resonant DC/DC converters," *IEEE Trans. Power Electron.*, vol. 27, no. 7, pp. 3266–3276, Jul. 2012.

[23] F. M. Ibanez, J. M. Echeverria, J. Vadillo, and L. Fontan, "State-plane analysis of anomalous step-up behavior in series-resonant converters," *IEEE J. Emerg. Sel. Topics Power Electron.*, vol. 4, no. 3, pp. 1026–1035, Sep. 2016.

[24] X. Li and A. K. S. Bhat, "Analysis and design of high-frequency isolated dual-bridge series resonant DC/DC converter," *IEEE Trans. Power Electron.*, vol. 25, no. 4, pp. 850–862, Apr. 2010.

[25] F. Ibanez, J. M. Echeverria, and L. Fontan, "Novel technique for bidirectional series-resonant DC/DC converter in discontinuous mode," *IET Power Electron*., vol. 6, no. 5, pp. 1019–1028, May 2013.

[26] F. M. Ibanez, J. M. Echeverria, J. Vadillo, and L. Fontan, "A step-up bidirectional series resonant DC/DC converter using a continuous current mode," *IEEE Trans. Power Electron.*, vol. 30, no. 3, pp. 1393–1402, Mar. 2015.

[27] F. Krismer, J. Biela, and J. W. Kolar, "A comparative evaluation of isolated bi-directional DC/DC converters with wide input and output voltage range," in *Proc. Fourtieth IAS Annu. Meeting. Conf. Record Industry App. Conf.*, Kowloon, Hong Kong, 2005, vol. 1, pp. 599–606.

[28] W. Chen, P. Rong, and Z. Lu, "Snubberless bidirectional DC–DC converter with new CLLC resonant tank featuring minimized switching loss," *IEEE Trans. Ind. Electron.*, vol. 57, no. 9, pp. 3075–3086, Sep. 2010.

[29] Z. U. Zahid, Z. M. Dalala, R. Chen, B. Chen, and J. Lai, "Design of bidirectional DC–DC resonant converter for vehicle-to-grid (V2G) applications," *IEEE Trans. Transp. Electrific.*, vol. 1, no. 3, pp. 232–244, Oct. 2015.

[30] J. Jung, H. Kim, J. Kim, M. Ryu, and J. Baek, "High efficiency bidirectional LLC resonant converter for 380V DC power distribution system using digital control scheme," in *Proc. 27th Annu. IEEE Appl. Power Electron. Conf. Expo.*, 2012, pp. 532–538.

[31] N. A. Kumar, R. Dhanalakshmi, and C. Gayithri, "Investigations on bidirectional resonant converters for renewable energy sources and energy storage systems," in *Proc. Int. Conf. Adv. Commun. Control Comput. Technologies*, 2016, pp. 396–401.

[32] A. N. Rahman, H. Chiu, and Y. Hsieh, "Design of wide input voltage range high step-up DC-DC converter based on secondary-side resonant tank full bridge LLC," in *Proc. 3rd Int. Conf. Intell. Green Building Smart Grid*, 2018, pp. 1–6.

[33] K. Tan, R. Yu, S. Guo, and A. Q. Huang, "Optimal design methodology of bidirectional LLC resonant DC/DC converter for solid state transformer application," in *Proc. 40th Annu. Conf. IEEE Ind. Electron. Soc.*, 2014, pp. 1657–1664.

[34] S. Ditze, "Steady-state analysis of the bidirectional CLLLC resonant converter in time domain," in *Proc. IEEE 36th Int. Telecommun. Energy Conf* ., 2014, pp. 1–9.

[35] E. Kim, J. Park, J. Joo, S. Lee, K. Kim, and Y. Kong, "Bidirectional DC-DC converter using secondary LLC resonant tank," in *Proc. IEEE Appl. Power Electron. Conf. Expo*., 2015, pp. 2104–2108.

[36] Y. Li, Y. Xing, Y. Lu, H. Wu, and P. Xu, "Performance analysis of a current-fed bidirectional LLC resonant converter," in *Proc. 42nd Annu. Conf. IEEE Ind. Electron. Soc.*, 2016, pp. 2486–2491.

[37] M. P. Foster, H. I. Sewell, C. M. Bingham, D. A. Stone, and D. Howe, "Methodologies for the design of LCC voltage-output resonant converters," *IEE Proc. Electric Power Appl.*, vol. 153, no. 4, pp. 559–567, Jul. 2006.

[38] J. A. Martin-Ramos, J. Diaz, A. M. Pernia, J. M. Lopera, and F. Nuno, "Dynamic and steady-state models for the PRC-LCC resonant topology with a capacitor as output filter," *IEEE Trans. Ind. Electron.*, vol. 54, no. 4, pp. 2262–2275, Aug. 2007.

[39] F. Musavi, M. Craciun, D. S. Gautam, W. Eberle, and W. G. Dunford, "An LLC resonant DC-DC converter for wide output voltage range battery charging applications," *IEEE Trans. Power Electron.*, vol. 28, no. 12, pp. 5437–5445, Dec. 2013.

[40] M. Joung, H. Kim, and J. Baek, "Dynamic analysis and optimal design of high efficiency full bridge LLC resonant converter for server power system," in *Proc. 27th Annu. IEEE Appl. Power Electron. Conf. Expo.*, 2012, pp. 1292–1297.

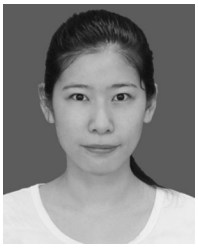

Yi Zhang was born in Qingdao, China, in 1989. She received the B.S. degree from the Harbin Institute of Technology, Weihai, China, in 2012, and the M.S. degree in 2014 from the Harbin Institute of Technology, Shenzhen, China, where she is currently working toward the Ph.D. degree in power electronics and power drives.

Her current research interests include power electronics, bidirectional dc/dc converter and aerospace power technology.

Donglai Zhang (Senior Member, IEEE) was born in Jilin, China, in 1973. He received the B.S., M.S., and Ph.D. degrees from the Harbin Institute of Technology, Harbin, China, in 1994, 1996, and 1999, respectively.

Since 2005, he has been a Professor at the Harbin Institute of Technology Shenzhen Graduate School. His research interests include analysis, modeling and control of power converters, digital control techniques for power electronic circuits, and grid-connected converters for renewable energy systems. In these research fields, he was leading several industrial and government projects.

Prof. Zhang is a member of the China Power Electronics Society. He is also a member of the IEEE.

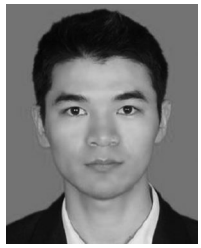

Jie Li was born in Shangrao, China, in 1995. He received the B.S. degree from the Jiang Xi Universiry of Science and Technology, China, in 2017, and the M.S. degree from the Harbin Institute of Technology, Shenzhen, China, in 2019.

He is currently working in State Grid Jiangxi Nanchang Power Supply Company. His current research interests include power electronics, bidirectional dc/dc converters, and power systems.

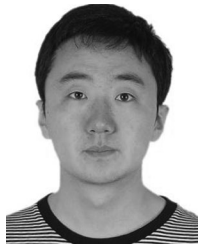

Hongyu Zhu was born in Harbin, China, in 1985. He received the B.S. degree from the Northeast Forestry University, Harbin, Heilongjiang, in 2007, and the M.S. and Ph.D. degrees from the Harbin Institute of Technology, Shenzhen Graduate School, China, in 2009 and 2015, respectively.

Since 2015, he has been a Senior Engineer at Shenzhen Aeropace New Power Technology Co., Ltd. His research interests include space power electronics, renewable energy systems and motion control. In these research fields, he was leading several industrial and government projects.